Report

Cell Reports

# Super-Resolution Microscopy Reveals the Native Ultrastructure of the Erythrocyte Cytoskeleton

## Graphical Abstract

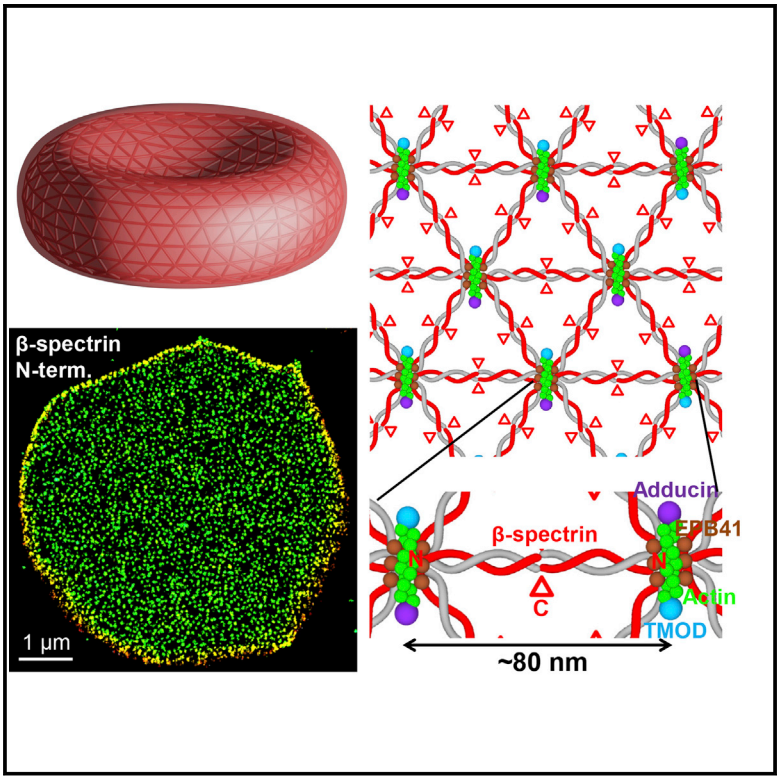


## Authors

Leiting Pan, Rui Yan, Wan Li, Ke Xu

## Correspondence

xuk@berkeley.edu

## In Brief

Pan et al. resolve the cytoskeletal organization in native erythrocytes using STORM super-resolution microscopy, revealing an ~80-nm junction-to-junction distance that is in agreement with relaxed spectrin tetramers and showing that the junctional complexes are partially occupied by actin and its capping proteins.

## Highlights

- Super-resolution microscopy resolves the cytoskeleton of intact erythrocytes
- Native erythrocyte cytoskeleton has an ~80-nm junction-to-junction distance
- Spectrin tetramers are relaxed rather than stretched/stressed in erythrocytes
- Actin and its capping proteins occupy subsets of junctional complexes

Pan et al., 2018, Cell Reports *22*, 1151–1158
January 30, 2018 
https://doi.org/10.1016/j.celrep.2017.12.107

CellPress

Cell Reports
Report



# Super-Resolution Microscopy Reveals the Native Ultrastructure of the Erythrocyte Cytoskeleton

Leiting Pan,[1,2] Rui Yan,[2] Wan Li,[2] and Ke Xu[2,3,4,*]
[1]Key Laboratory of Weak-Light Nonlinear Photonics, Ministry of Education, School of Physics and TEDA Institute of Applied Physics, Nankai University, Tianjin 300071, China
[2]Department of Chemistry, University of California, Berkeley, Berkeley, CA 94720, USA
[3]Chan Zuckerberg Biohub, San Francisco, CA 94158, USA
[4]Lead Contact
*Correspondence: xuk@berkeley.edu
https://doi.org/10.1016/j.celrep.2017.12.107

## SUMMARY

**The erythrocyte cytoskeleton is a textbook prototype for the submembrane cytoskeleton of metazoan cells. While early experiments suggest a triangular network of actin-based junctional complexes connected by ~200-nm-long spectrin tetramers, later studies indicate much smaller junction-to-junction distances in the range of 25-60 nm. Through super-resolution microscopy, we resolve the native ultrastructure of the cytoskeleton of membrane-preserved erythrocytes for the N and C termini of β-spectrin, F-actin, protein 4.1, tropomodulin, and adducin. This allows us to determine an ~80-nm junction-to-junction distance, a length consistent with relaxed spectrin tetramers and theories based on spectrin abundance. Through two-color data, we further show that the cytoskeleton meshwork often contains nanoscale voids where the cell membrane remains intact and that actin filaments and capping proteins localize to a subset of, but not all, junctional complexes. Together, our results call for a reassessment of the structure and function of the submembrane cytoskeleton.**

## INTRODUCTION

Devoid of organelles and other cytoskeletal components, the human erythrocyte relies heavily on its membrane cytoskeleton to maintain structural stability and regulate membrane proteins. Understanding the structure and function of this key cytoskeletal system—which also often serves as a textbook prototype for the cortical (submembrane) cytoskeleton of metazoan cells—is, therefore, of fundamental importance.

Current models often depict the erythrocyte cytoskeleton as a two-dimensional triangular meshwork (Figure 1A) composed of rod-shaped spectrin tetramers that connect at junctional complexes consisting of short actin filaments, adducin, tropomodulin, protein 4.1, and associated proteins (Alberts et al., 2015; Baines, 2010; Bennett and Gilligan, 1993; Lux, 2016). Estimates based on the copy numbers of spectrin molecules and the total area of the erythrocyte membrane have suggested the edges of the meshwork (*d* in Figure 1B) to be 70–80 nm (Lux, 2016; Vertessy and Steck, 1989; Waugh, 1982), close to the root-mean-square end-to-end distance of relaxed spectrin tetramers predicted from the experimental viscosity data of spectrin dimers (Stokke et al., 1985).

However, it remains a challenge to experimentally determine the actual ultrastructure of the erythrocyte cytoskeleton. Electron microscopy (EM) data of spread erythrocyte cytoskeletons show ~200-nm meshwork edges (Byers and Branton, 1985; Liu et al., 1987; McGough and Josephs, 1990), consistent with the extended full length of spectrin tetramers (Shotton et al., 1979). Conversely, results from quick-freezing, deep etching, and rotary replication (QFDERR) and atomic force microscopy (AFM) of non-spread cytoskeleton suggest substantially denser meshworks of conflicting average edge length, *d*, in the wide range of 25–60 nm (Ohno et al., 1994; Swihart et al., 2001; Takeuchi et al., 1998; Ursitti et al., 1991; Ursitti and Wade, 1993). A recent study using cryo-electron tomography of the membrane-removed cytoskeleton of mouse erythrocytes indicated a ~46-nm edge length (Nans et al., 2011).

Difficulty in obtaining the native ultrastructure of the erythrocyte cytoskeleton arises from the extensive sample processing necessary for previous studies, in which samples were often dried and/or membrane removed. By reaching ~20-nm optical resolution, recent advances in super-resolution fluorescence microscopy (Hell, 2007; Huang et al., 2010) offer new opportunities: ultrastructure can now be probed in wet and live cells with minimal sample processing. In particular, recent work led to the discovery of a periodically arranged, spectrin-actin-based submembrane cytoskeleton in neuronal cells (Xu et al., 2013). There, spectrin tetramers connect actin-based junctional complexes to form one-dimensional (D'Este et al., 2015, 2016, 2017; Ganguly et al., 2015; Han et al., 2017; He et al., 2016; Leterrier et al., 2015; Xu et al., 2013; Zhong et al., 2014) and two-dimensional (D'Este et al., 2017; Han et al., 2017) lattices with 180–190 nm periodicity. This value agrees with the extended length of spectrin tetramers (Bennett et al., 1982; Shotton et al., 1979), as well as the aforementioned EM results of spread erythrocyte cytoskeleton but contrasts with the substantially smaller grid sizes found in non-spread erythrocytes.

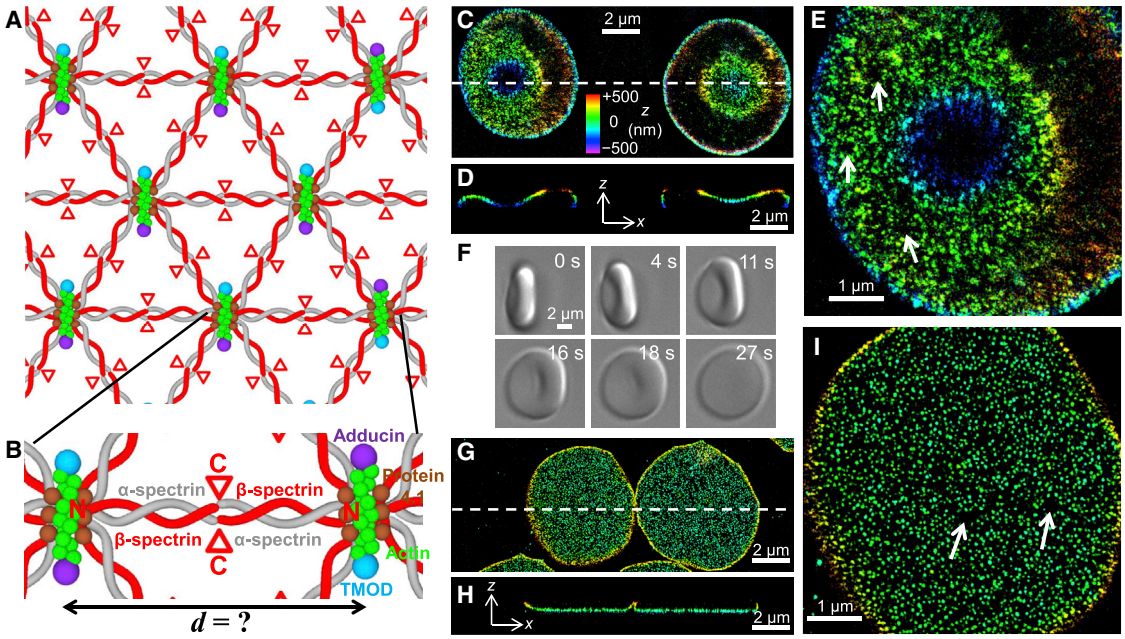


**Figure 1. Super-Resolution Microscopy for the Cytoskeleton of Membrane-Preserved Erythrocytes**

(A) Current model of the spectrin-actin-based cytoskeleton of erythrocytes.

(B) A close-up of an edge of the cytoskeletal network. Rod-like spectrin tetramers are connected by junctional complexes containing short actin filaments, adducin, tropomodulin, and protein 4.1, thus forming a quasi-triangle network with edge length *d*. The N termini of β-spectrin bind to actin at the junctions, and the C termini of β-spectrin are at the centers of the network edges (open triangles).

(C) 3D-STORM super-resolution image of intact human erythrocytes that were first chemically fixed and then immunolabeled for tropomodulin. Color is used to present the depth (*z*) information.

(D) Virtual cross-section of the 3D-STORM data in the *xz* plane along the white dash line in (C).

(E) Zoom-in of the cell on the left in (C). Arrows point to nanoscale tropomodulin-deficient voids.

(F) DIC microscopy recording of the bottom-flattening process of a live erythrocyte.

(G) 3D-STORM super-resolution image of tropomodulin in bottom-flattened erythrocytes.

(H) Virtual cross-section of the 3D-STORM data in the *xz* plane along the white dash line in (G).

(I) Zoom-in of the cell on the left in (G). Arrows indicate nanoscale tropomodulin-deficient voids.

Here, we initiated a systematic super-resolution microscopy study of the intact cytoskeleton of membrane-preserved human erythrocytes at ~25-nm spatial resolution. This allowed us to reveal structural arrangements that are markedly different from previous experimental results of both erythrocytes and neuronal cells.

## RESULTS

We started with human erythrocytes that were first chemically fixed and then immunolabeled for super-resolution microscopy (Figures 1C–1E). Three-dimensional stochastic optical reconstruction microscopy (3D-STORM) (Huang et al., 2008; Rust et al., 2006) showed that the biconcave-disk shape of the erythrocytes led to suboptimal resolution and complicated data interpretation as the cell surface frequently came in and out of the ~800-nm focal range of 3D-STORM (Huang et al., 2008).

To overcome this limitation, we developed an alternative approach in which live erythrocytes were first allowed to adhere to a polylysine-coated coverslip for a few minutes before subsequent fixation and labeling. Differential interference contrast (DIC) microscopy showed that, upon contact with the coverslip, the bottom membrane of erythrocytes spread flat within seconds (Figure 1F). 3D-STORM results indicated that the bottom membrane cytoskeleton was flat down to the axial resolution limit (~50 nm) (Huang et al., 2008) and that this cytoskeletal layer quickly rose in height at the cell edges to outside of the focal range (Figures 1G and 1H). Consequently, only the cytoskeleton associated with the bottom membrane was imaged. The possibility to perform 3D-STORM at the coverslip surface allowed us to achieve optimal image quality. Tropomodulin labeling showed up as individual clusters that were ~11 nm in SD and ~26 nm in full width at half maximum (FWHM), in good agreement with the in-plane resolution of 3D-STORM (~25 nm) (Huang et al., 2008). Similar cluster density and structural features were found for the bottom-flattened cells (Figure 1I) and the fixation-first cells (Figure 1E). With this approach, we examined the ultrastructure of six different targets of the erythrocyte cytoskeleton in membrane-preserved cells.

For spectrin-related targets that should localize to junctional complexes, the N termini (actin-binding domain) of β-spectrin and protein 4.1 both showed up as clusters with relatively uniform distribution across the cell membrane at high density (Figures 2A, 2B, 2D, and 2E; Figure S1). Clusters showed apparent

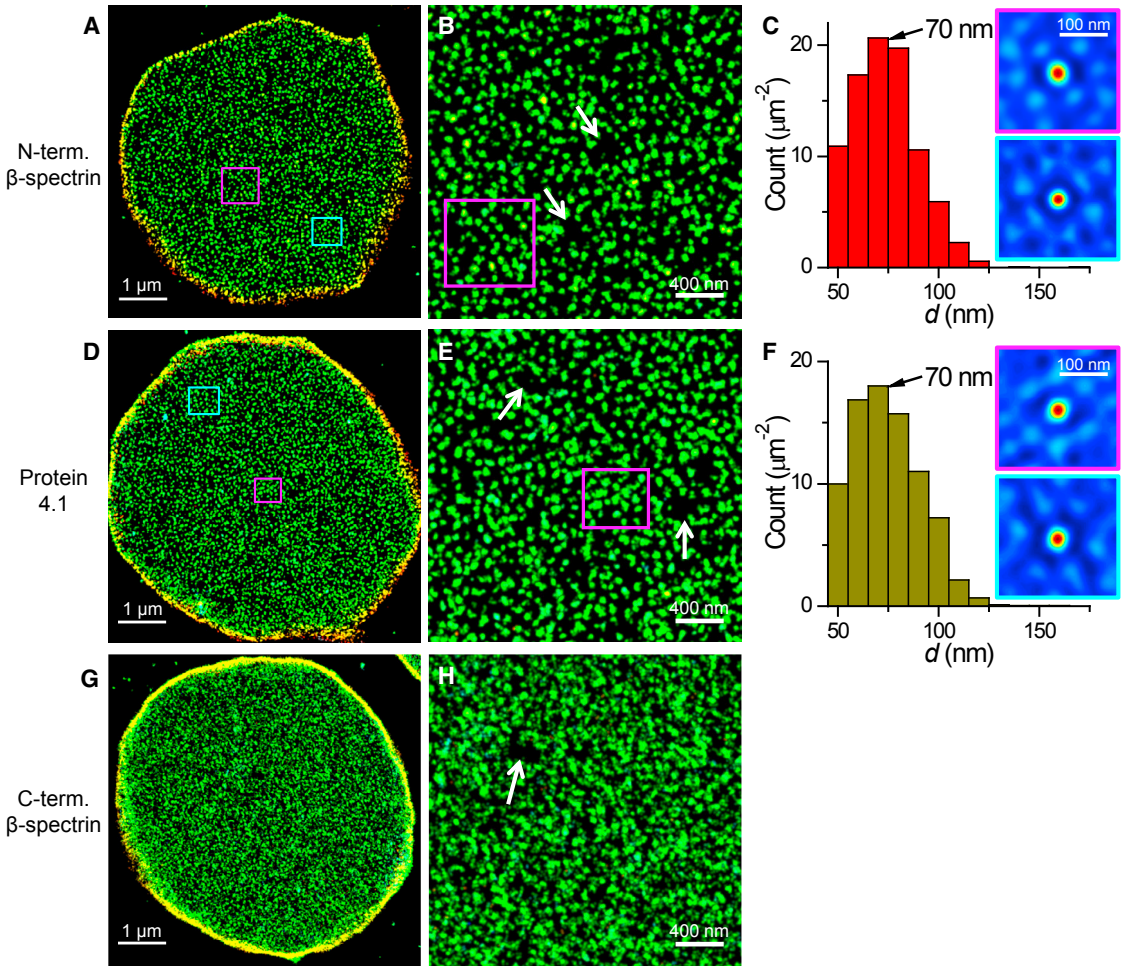


**Figure 2. 3D-STORM Results of β-Spectrin and Protein 4.1 in Membrane-Preserved Erythrocytes**

(A) 3D-STORM image of the N terminus (actin-binding domain) of β-spectrin.

(B) Zoom-in of (A).

(C) Distribution of distances between nearest neighbors of β-spectrin clusters in (A). Insets: two-dimensional autocorrelation for the magenta- and cyan-boxed regions in (A) and (B).

(D) 3D-STORM image of protein 4.1.

(E) Zoom-in of (D).

(F) Distribution of distances between nearest neighbors of protein 4.1 clusters in (D). Insets: Two-dimensional autocorrelation for the magenta- and cyan-boxed regions in (D) and (E).

(G) 3D-STORM image of the C terminus of β-spectrin (center of spectrin tetramer).

(H) Zoom-in of (G).The same color scale as Figure 1C is used to present the depth (*z*) information of all images. White arrows in (B), (E), and (H) point to nanoscale voids.

See also Figure S1.

sizes of ~30 nm in FWHM, a value just slightly larger than the in-plane resolution of 3D-STORM (~25 nm). Considering that each cluster represents the converging point of ~6 spectrin tetramers (Figures 1A and 1B), this result suggests that the N termini of the ~6 β-spectrin molecules meet at the same position within ~20 nm. Similar packed arrangements were observed for the clusters of both targets, with generally uniform center-to-center distances between adjacent clusters. Statistics of distances between nearest neighbors (Figures 2C and 2F) gave distributions of ~50–100 nm, with peaks at ~70 nm for both targets, and consistent results were obtained for different cells (Figure S1). Two-dimensional autocorrelations of small regions of the images (D'Este et al., 2017; Han et al., 2017) gave distorted hexagonal lattices with ~70–90 nm distances between the 0th and 1st peaks (insets of Figures 2C and 2F), indicative of local triangular lattices at such spacings that are substantially smaller than the fully stretched length of spectrin tetramers (~200 nm). Accompanying this dense arrangement, however, voids ~200 nm in size were frequently observed for both targets (white arrows in Figures 2B and 2E; Figure S1). Together, the observed cluster density was comparable for both targets at ~110/$\mu m^2$.

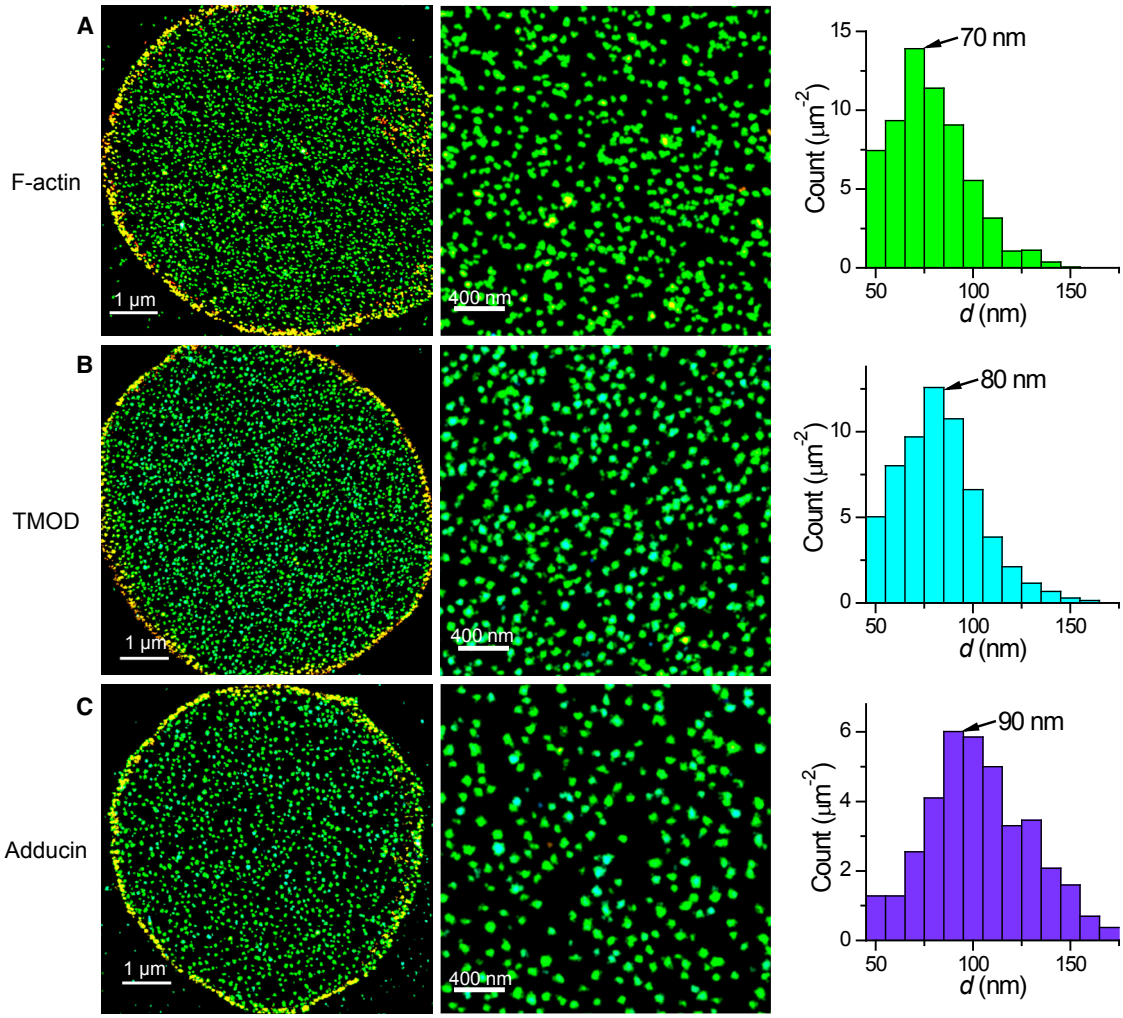


**Figure 3. 3D-STORM Results of Actin Filaments and Actin-Capping Proteins in Membrane-Preserved Erythrocytes**

(A) Results of phalloidin-labeled actin filaments.

(B) Results of tropomodulin.

(C) Results of adducin.

Left, center, and right panels of (A)–(C) give 3D-STORM images at low and high magnifications and distribution of distances between nearest neighbors of clusters, respectively.

See also Figures S2, S3, and S4.

We next examined the structural organization of the C terminus of β-spectrin, which should correspond to the center of each spectrin tetramer (Figure 1B). A very high labeling density was observed (Figures 2G and 2H; Figure S1), and distances between adjacent clusters were difficult to quantify. This result is expected, as the area density of the centers of spectrin tetramers should, in principle, be 3-fold higher than junctional complexes, and the organization is more complicated than a simple triangular lattice (Figure 1A). Despite this high density, voids ~200 nm in size (arrows in Figures 2H and S1) were still frequently observed, similar to what we found for the N termini of β-spectrin and protein 4.1.

In contrast to the dense, packed arrangements of spectrin and protein 4.1, actin filaments (labeled by dye-tagged phalloidin [Xu et al., 2012]) (Figures 3A and S2), as well as two proteins that respectively cap the two ends of the actin filaments—namely, tropomodulin and adducin (Figures 3B and 3C, and S2)—exhibited lower cluster densities of 80/$\mu m^2$, 70/$\mu m^2$, and 45/$\mu m^2$, respectively. Interestingly, though presented at lower densities, statistics of distances between nearest neighbors still yielded peaks at 70–90 nm for all three actin-related targets (Figures 3 and S2), comparable to that of the N termini of β-spectrin and protein 4.1 (Figures 2C, 2F, and S1). This result may be explained as that the actin-related targets occupy a subset of the same underlying junctions as the N terminus of β-spectrin and protein 4.1 and that the measurement of the distance between nearest neighbors is insensitive to occupancy. To test this possibility, we simulated junction structures based on a triangular lattice

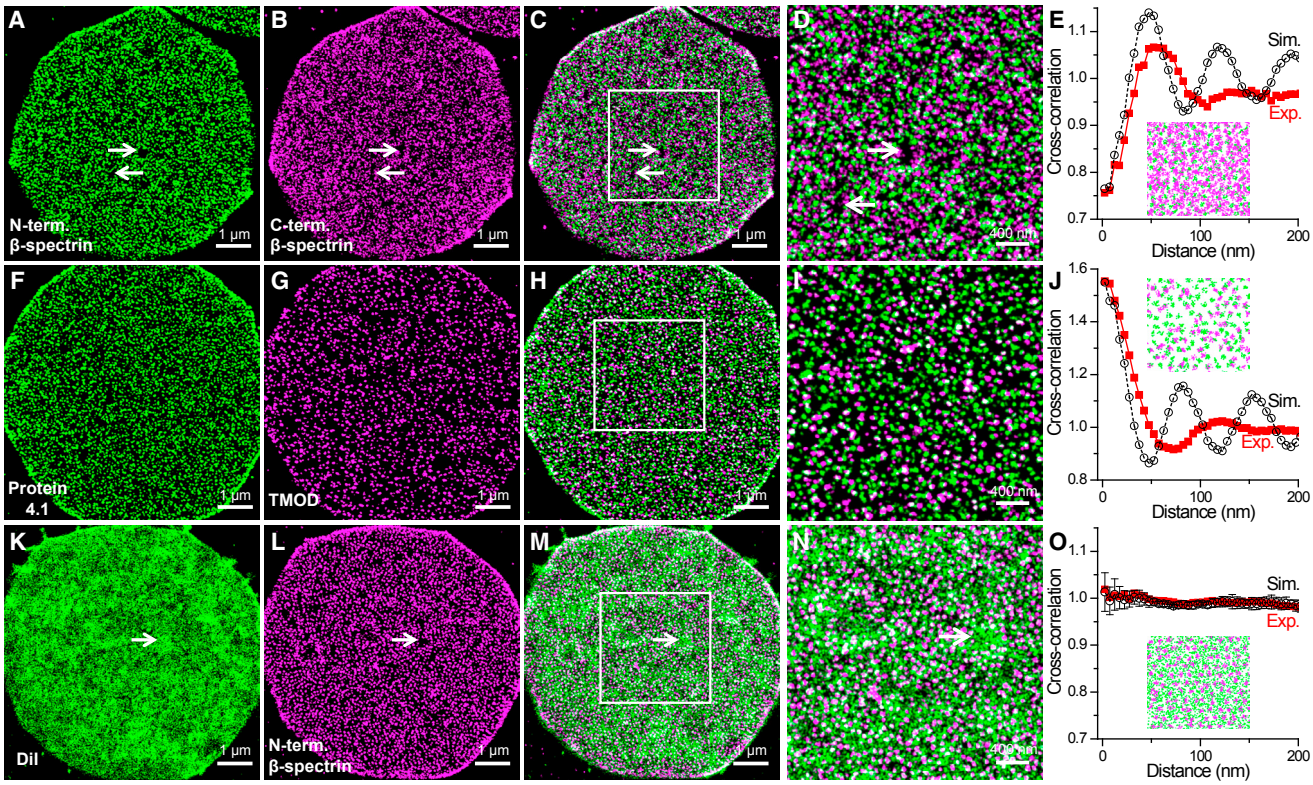


**Figure 4. Two-Color STORM Results of Membrane-Preserved Erythrocytes**

(A–C) Separate STORM images of the N terminus (A; green) and C terminus (B; magenta) of β-spectrin, and overlaid STORM image (C).

(D) Zoom-in of the box in (C). Arrows point to co-localized nanoscale voids.

(E) Calculated two-dimensional cross-correlations between the two channels at different intermolecular distances based on the experimental (red) and simulated (black) data.

(F–H) Separate STORM images of protein 4.1 (F; green) and tropomodulin (G; magenta) and overlaid STORM image (H).

(I) Zoom-in of the box in (H).

(J) Calculated two-dimensional cross-correlations between the two channels for the experimental (red) and simulated (black) data. Simulation was based on 60% sites of protein 4.1 being occupied by tropomodulin.

(K–M) Separate STORM images of the membrane dye CM-DiI (K; green) and N terminus of β-spectrin (L; magenta), and overlaid STORM image (M).

(N) Zoom-in of the box in (K). Arrow points to a nanoscale void in the spectrin image.

(O) Calculated two-dimensional cross-correlations between the two channels for the experimental (red) and simulated (black) data. Error bars indicate the SD between six sets of simulated data.

of 85-nm edges, with added random positional scattering of each junction, and compared the distribution of junction-to-junction distances between nearest neighbors when the lattices were 90% or 25% occupied. Comparable peak positions at ~70–80 nm were found for the two scenarios (Figure S3), in line with our experimental observations.

We next carried out two-color STORM to elucidate the structural relationships between different targets. Labeling to the N and C termini of β-spectrin, which should localize to the vertices and edges of the spectrin meshwork, respectively (Figures 1A and 1B), showed complimentary patterns at the nanoscale, so that the latter filled into the gaps between adjacent labeling of the former (Figures 4A–4D). Two-dimensional pairwise cross-correlation calculation (Sengupta et al., 2011; Stone and Veatch, 2015) between the two color channels (Figure 4E), as performed by a modified algorithm for single-molecule localizations (Supplemental Experimental Procedures), showed a minimum value of ~0.75 at zero intermolecular distance, and this value quickly rose to ~1 within ~50 nm, thus further confirming complimentary patterns at the nanoscale. This behavior matched well to simulated results based on an 85-nm triangular lattice (Figure 4E and inset). Notably, while the N and C termini of β-spectrin labeling are complementary to each other in the meshwork, the aforementioned ~200-nm voids often co-localized for the two channels (arrows in Figures 4A–4D), indicating that these regions are, indeed, devoid of cytoskeleton.

Meanwhile, two-color results of protein 4.1 and tropomodulin, two targets that should both locate to junctional complexes, showed that the former formed a denser and more uniform array, whereas the latter co-localized with, or was in close proximity to, a subset of the clusters of the former (Figures 4F–4I). Cross-correlation calculation between the two color channels showed a maximum of ~1.6 at zero intermolecular distance, which quickly dropped to ~1 within ~50 nm, thus further

confirming co-localization at the nanoscale and matching well with simulated results (Figure 4J).

To understand whether the cytoskeletal ultrastructure, including the ~200-nm-sized voids we observed, modulates the structure of the cell membrane, we next performed two-color STORM using the N terminus of β-spectrin to represent the cytoskeleton and the lipid marker CM-DiI for STORM of the membrane (Shim et al., 2012; Wojcik et al., 2015). The cell membrane was continuously labeled by CM-DiI (Figure 4K). Although nanoscale inhomogeneity was noted for local labeling intensity, a phenomenon also observed in other cell types (Shim et al., 2012; Wojcik et al., 2015), the variations were independent of the local cytoskeleton ultrastructure (Figures 4K–4N). In particular, the ~200-nm cytoskeletal voids did not correspond to voids or weaker labeling of the membrane (arrows in Figures 4K–4N), indicating that the cell membrane remains intact over these areas. Cross-correlation calculation gave values ~1 for all intermolecular distances (Figure 4O), confirming no specific structural relationships between the two color channels.

## DISCUSSION

Through 3D-STORM, we have resolved the native ultrastructure of the cytoskeleton of membrane-preserved human erythrocytes, with all sample processing and imaging procedures carried out under fully hydrated and buffered conditions. Molecular specificity was achieved for six targets through fluorescent labeling, thus enabling quantitative examinations of their respective structural organizations, as well as their relative arrangements versus each other and the cell membrane, at the nanoscale.

The ~80-nm edge length we found for the cytoskeletal meshwork is less than one half of the classical results from EM of spread erythrocyte cytoskeletons (Byers and Branton, 1985; Liu et al., 1987; McGough and Josephs, 1990). This result indicates that the spectrin tetramers in spread preparations are artificially extended. Regarding the vastly different results (25–60 nm) obtained from non-spread preparations, QFDERR and AFM often work with heavily fixed and dried samples, and the limited molecular specificity makes it difficult to ascertain which structural features correspond to actual edges connecting junctional complexes (Ohno et al., 1994; Swihart et al., 2001; Takeuchi et al., 1998; Ursitti et al., 1991; Ursitti and Wade, 1993). While recent work with cryo-electron tomography partially overcomes these limitations, cell membrane is removed before centrifugal fractionation on a sucrose gradient, and cytoskeletons from the top and bottom membranes are juxtaposed in the preparation (Nans et al., 2011), thus adding uncertainties to results.

Remarkably, the ~80-nm length we observed matches well that estimated from the total amount of spectrin molecules in the erythrocyte membrane (Lux, 2016; Vertessy and Steck, 1989; Waugh, 1982), as well as the predicted root-mean-square end-to-end distance of relaxed spectrin tetramers (Stokke et al., 1985). Our results thus suggest that the cytoskeleton of resting erythrocytes is in a relaxed state close to thermodynamic equilibrium. This may be functionally helpful for erythrocytes to accommodate both expansion and compression as they undergo frequent structural deformation during circulation.

Our results, however, raise the counter-question of why the recently discovered spectrin-actin-based membrane cytoskeleton of neuronal cells (D'Este et al., 2015, 2016, 2017; Ganguly et al., 2015; Han et al., 2017; He et al., 2016; Leterrier et al., 2015; Xu et al., 2013; Zhong et al., 2014), obtained under similar super-resolution settings, is characterized by an 180- to 190-nm periodicity that matches the extended full length of spectrin tetramers (~195 nm) (Bennett et al., 1982; Shotton et al., 1979). Although, in neuronal cells, αII-βII spectrin tetramers dominate (Baines, 2010; Bennett et al., 1982; Levine and Willard, 1981)—as opposed to αI-βI tetramers in erythrocytes—the protein structures, including extended lengths of the tetramers (Bennett et al., 1982), are highly similar. The contrasting lengths of spectrin tetramers in erythrocytes and neuronal processes thus suggest that the latter is under constant tensile stress (Zhang et al., 2017). This force may be provided by the microtubule and neurofilament cytoskeletal systems that jam-pack inside neuronal processes, which are absent in erythrocytes. Indeed, it has been shown that the 180- to 190-nm spectrin periodicity in neurons relies on intact microtubules (Zhong et al., 2014). In addition, in neuronal processes, the spectrin tetramers are bundled by actin rings and aligned in the same direction: this synergistic arrangement may increase the effective rigidity of spectrin tetramers (Lai and Cao, 2014).

Despite the small grid size, our results further revealed that the dense erythrocyte cytoskeleton often contained voids ~200 nm in size. Two-color STORM results indicated that these nanoscale voids corresponded to regions devoid of cytoskeletal components but that their existence did not affect the integrity of the plasma membrane. Such imperfections in the cytoskeletal meshwork may behave as structural weak points to facilitate quick changes of the erythrocyte shape during circulation. Previous work on the AFM of erythrocytes under physiological conditions (Nowakowski et al., 2001) has occasionally noted nanoscale "dimples" where the plasma membrane is pushed further into the cell by the AFM tip, indicative of cytoskeletal defects that weaken the local membrane. Scrutiny of previous EM and AFM results on the erythrocyte cytoskeleton occasionally identified voids that could be consistent with our results (Liu et al., 1987; Nans et al., 2011; Ohno et al., 1994; Takeuchi et al., 1998); however, it is difficult to determine whether these structures are native or due to the extensive sample processing involved, and the viewing windows are often small when compared to our whole-cell STORM images.

While the locations of the different targets revealed by STORM in this work were consistent with that deduced from the *in vitro* interactions of purified proteins (Figures 1A and 1B), the actual structural arrangements, including occupancies, of different targets have been difficult to visualize in cells. In our results, actin filaments and actin-capping proteins, tropomodulin and adducin, localized to a subset of the junctional complexes. Previous work has shown that phalloidin labeling of fixed cells does not visualize the presumably less stable, periodic actin cytoskeleton in early-stage neurons as detected in live cells by a jasplakinolide-based stain (D'Este et al., 2015). We found that, when at rest in a buffer, actin filaments in the erythrocyte were stable and resistant to actin-destabilizing drugs (Figure S4), a result in agreement with previous diffraction-limited microscopy results

(Betz et al., 2009; Gokhin et al., 2015). Assuming that these stable filaments and associated proteins are well preserved in fixation, the observed disparity in their labeling when compared to that of protein 4.1 and the N and C termini of β-spectrin indicates that the cytoskeletal meshwork remains stable as the actin filaments and actin-capping proteins are absent for a subset of the junctional complexes. It is conceivable, however, that junctions without bound actin filaments may act as weak points to initiate the aforementioned nanoscale cytoskeletal voids.

Finally, while our results indicated that the structural organization of the erythrocyte cytoskeleton does not possess long-range orders as neurons, aspects of the structure may be, to a first-order approximation, captured by a triangular lattice of 85-nm grid length with random removal and scattering of nodes. Together, our super-resolution results thus call for both experimental and theoretical reassessments of the structure and function of the erythrocyte cytoskeleton and, more generally, the spectrin-actin-based cortical cytoskeleton of metazoan cells.

## EXPERIMENTAL PROCEDURES

### Sample Preparation

Erythrocytes were adhered to polylysine-coated glass coverslips for chemical fixation and immunofluorescence labeling. See Supplemental Experimental Procedures for details.

### STORM Imaging

3D-STORM imaging (Huang et al., 2008; Rust et al., 2006) was carried out on a home-built setup, as described in Wojcik et al. (2015). Most of the labeled dye molecules in the sample were photoswitched into a dark state, and fluorescence images of the remaining, sparsely distributed, emitting single molecules were recorded and super-localized over ~50,000 camera frames. A cylindrical lens differently elongated single-molecule images based on the depth (z) position. 3D-STORM images were reconstructed according to previously described methods (Huang et al., 2008; Rust et al., 2006), in which the centroid positions and ellipticities of each single-molecule image provided the lateral and axial positions, respectively. See Supplemental Experimental Procedures for details.

### Data Analysis and Modeling

Two-dimensional cross-correlation analysis (Sengupta et al., 2011; Stone and Veatch, 2015) was performed by calculating the pairwise intermolecular distances between single molecules identified in the two color channels. The distance distribution was normalized by results generated from multiple sets of molecules randomly distributed in the same area. Consequently, the resultant normalized cross-correlation amplitudes at given displacements indicate correlation and anti-correlation of the two color channels for values >1 and <1, respectively. Simulations of the cytoskeleton network were based on a triangular lattice with 85-nm-long edges, with added random shifts to the vertices and edge centers. Targets at the junctional complexes occupied a random fraction of the vertices. See Supplemental Experimental Procedures for details.

## SUPPLEMENTAL INFORMATION

Supplemental Information includes Supplemental Experimental Procedures and four figures and can be found with this article online at https://doi.org/10.1016/j.celrep.2017.12.107.

## ACKNOWLEDGMENTS

This work was supported by the National Natural Science Foundation of China (no. 11574165), the PCSIRT (no. IRT_13R29), the 111 Project (no. B07013), the Pew Biomedical Scholars Award, and the Packard Fellowships for Science and Engineering. K.X. is a Chan Zuckerberg Biohub Investigator.

## AUTHOR CONTRIBUTIONS

L.P. and R.Y. conducted experiments. L.P., R.Y., W.L., and K.X. analyzed data. K.X. supervised the project.

## DECLARATION OF INTERESTS

The authors declare no competing interests.

Received: August 20, 2017
Revised: November 23, 2017
Accepted: December 29, 2017
Published: January 30, 2018

## REFERENCES

Alberts, B., Johnson, A., Lewis, J., Morgan, D., Raff, M., Roberts, K., and Walter, P. (2015). Molecular Biology of the Cell, Sixth Edition (New York: Garland Science).

Baines, A.J. (2010). The spectrin-ankyrin-4.1-adducin membrane skeleton: adapting eukaryotic cells to the demands of animal life. Protoplasma *244*, 99–131.

Bennett, V., and Gilligan, D.M. (1993). The spectrin-based membrane skeleton and micron-scale organization of the plasma membrane. Annu. Rev. Cell Biol. *9*, 27–66.

Bennett, V., Davis, J., and Fowler, W.E. (1982). Brain spectrin, a membrane-associated protein related in structure and function to erythrocyte spectrin. Nature *299*, 126–131.

Betz, T., Lenz, M., Joanny, J.F., and Sykes, C. (2009). ATP-dependent mechanics of red blood cells. Proc. Natl. Acad. Sci. USA *106*, 15320–15325.

Byers, T.J., and Branton, D. (1985). Visualization of the protein associations in the erythrocyte membrane skeleton. Proc. Natl. Acad. Sci. USA *82*, 6153–6157.

D'Este, E., Kamin, D., Göttfert, F., El-Hady, A., and Hell, S.W. (2015). STED nanoscopy reveals the ubiquity of subcortical cytoskeleton periodicity in living neurons. Cell Rep. *10*, 1246–1251.

D'Este, E., Kamin, D., Velte, C., Göttfert, F., Simons, M., and Hell, S.W. (2016). Subcortical cytoskeleton periodicity throughout the nervous system. Sci. Rep. *6*, 22741.

D'Este, E., Kamin, D., Balzarotti, F., and Hell, S.W. (2017). Ultrastructural anatomy of nodes of Ranvier in the peripheral nervous system as revealed by STED microscopy. Proc. Natl. Acad. Sci. USA *114*, E191–E199.

Ganguly, A., Tang, Y., Wang, L., Ladt, K., Loi, J., Dargent, B., Leterrier, C., and Roy, S. (2015). A dynamic formin-dependent deep F-actin network in axons. J. Cell Biol. *210*, 401–417.

Gokhin, D.S., Nowak, R.B., Khoory, J.A., Piedra Ade, L., Ghiran, I.C., and Fowler, V.M. (2015). Dynamic actin filaments control the mechanical behavior of the human red blood cell membrane. Mol. Biol. Cell *26*, 1699–1710.

Han, B., Zhou, R., Xia, C., and Zhuang, X. (2017). Structural organization of the actin-spectrin-based membrane skeleton in dendrites and soma of neurons. Proc. Natl. Acad. Sci. USA *114*, E6678–E6685.

He, J., Zhou, R., Wu, Z., Carrasco, M.A., Kurshan, P.T., Farley, J.E., Simon, D.J., Wang, G., Han, B., Hao, J., et al. (2016). Prevalent presence of periodic actin-spectrin-based membrane skeleton in a broad range of neuronal cell types and animal species. Proc. Natl. Acad. Sci. USA *113*, 6029–6034.

Hell, S.W. (2007). Far-field optical nanoscopy. Science *316*, 1153–1158.

Huang, B., Wang, W., Bates, M., and Zhuang, X. (2008). Three-dimensional super-resolution imaging by stochastic optical reconstruction microscopy. Science *319*, 810–813.

Huang, B., Babcock, H., and Zhuang, X. (2010). Breaking the diffraction barrier: super-resolution imaging of cells. Cell *143*, 1047–1058.

Lai, L., and Cao, J. (2014). Spectrins in axonal cytoskeletons: dynamics revealed by extensions and fluctuations. J. Chem. Phys. *141*, 015101.

Leterrier, C., Potier, J., Caillol, G., Debarnot, C., Rueda Boroni, F., and Dargent, B. (2015). Nanoscale architecture of the axon initial segment reveals an organized and robust scaffold. Cell Rep. *13*, 2781–2793.

Levine, J., and Willard, M. (1981). Fodrin: axonally transported polypeptides associated with the internal periphery of many cells. J. Cell Biol. *90*, 631–642.

Liu, S.C., Derick, L.H., and Palek, J. (1987). Visualization of the hexagonal lattice in the erythrocyte membrane skeleton. J. Cell Biol. *104*, 527–536.

Lux, S.E., 4th. (2016). Anatomy of the red cell membrane skeleton: unanswered questions. Blood *127*, 187–199.

McGough, A.M., and Josephs, R. (1990). On the structure of erythrocyte spectrin in partially expanded membrane skeletons. Proc. Natl. Acad. Sci. USA *87*, 5208–5212.

Nans, A., Mohandas, N., and Stokes, D.L. (2011). Native ultrastructure of the red cell cytoskeleton by cryo-electron tomography. Biophys. J. *101*, 2341–2350.

Nowakowski, R., Luckham, P., and Winlove, P. (2001). Imaging erythrocytes under physiological conditions by atomic force microscopy. Biochim. Biophys. Acta *1514*, 170–176.

Ohno, S., Terada, N., Fujii, Y., and Ueda, H. (1994). Membrane skeleton in fresh unfixed erythrocytes as revealed by a rapid-freezing and deep-etching method. J. Anat. *185*, 415–420.

Rust, M.J., Bates, M., and Zhuang, X. (2006). Sub-diffraction-limit imaging by stochastic optical reconstruction microscopy (STORM). Nat. Methods *3*, 793–795.

Sengupta, P., Jovanovic-Talisman, T., Skoko, D., Renz, M., Veatch, S.L., and Lippincott-Schwartz, J. (2011). Probing protein heterogeneity in the plasma membrane using PALM and pair correlation analysis. Nat. Methods *8*, 969–975.

Shim, S.H., Xia, C., Zhong, G., Babcock, H.P., Vaughan, J.C., Huang, B., Wang, X., Xu, C., Bi, G.Q., and Zhuang, X. (2012). Super-resolution fluorescence imaging of organelles in live cells with photoswitchable membrane probes. Proc. Natl. Acad. Sci. USA *109*, 13978–13983.

Shotton, D.M., Burke, B.E., and Branton, D. (1979). The molecular structure of human erythrocyte spectrin. Biophysical and electron microscopic studies. J. Mol. Biol. *131*, 303–329.

Stokke, B.T., Mikkelsen, A., and Elgsaeter, A. (1985). Human erythrocyte spectrin dimer intrinsic viscosity: temperature dependence and implications for the molecular basis of the erythrocyte membrane free energy. Biochim. Biophys. Acta *816*, 102–110.

Stone, M.B., and Veatch, S.L. (2015). Steady-state cross-correlations for live two-colour super-resolution localization data sets. Nat. Commun. *6*, 7347.

Swihart, A.H., Mikrut, J.M., Ketterson, J.B., and Macdonald, R.C. (2001). Atomic force microscopy of the erythrocyte membrane skeleton. J. Microsc. *204*, 212–225.

Takeuchi, M., Miyamoto, H., Sako, Y., Komizu, H., and Kusumi, A. (1998). Structure of the erythrocyte membrane skeleton as observed by atomic force microscopy. Biophys. J. *74*, 2171–2183.

Ursitti, J.A., and Wade, J.B. (1993). Ultrastructure and immunocytochemistry of the isolated human erythrocyte membrane skeleton. Cell Motil. Cytoskeleton *25*, 30–42.

Ursitti, J.A., Pumplin, D.W., Wade, J.B., and Bloch, R.J. (1991). Ultrastructure of the human erythrocyte cytoskeleton and its attachment to the membrane. Cell Motil. Cytoskeleton *19*, 227–243.

Vertessy, B.G., and Steck, T.L. (1989). Elasticity of the human red cell membrane skeleton. Effects of temperature and denaturants. Biophys. J. *55*, 255–262.

Waugh, R.E. (1982). Temperature dependence of the yield shear resultant and the plastic viscosity coefficient of erythrocyte membrane. Implications about molecular events during membrane failure. Biophys. J. *39*, 273–278.

Wojcik, M., Hauser, M., Li, W., Moon, S., and Xu, K. (2015). Graphene-enabled electron microscopy and correlated super-resolution microscopy of wet cells. Nat. Commun. *6*, 7384.

Xu, K., Babcock, H.P., and Zhuang, X. (2012). Dual-objective STORM reveals three-dimensional filament organization in the actin cytoskeleton. Nat. Methods *9*, 185–188.

Xu, K., Zhong, G., and Zhuang, X. (2013). Actin, spectrin, and associated proteins form a periodic cytoskeletal structure in axons. Science *339*, 452–456.

Zhang, Y., Abiraman, K., Li, H., Pierce, D.M., Tzingounis, A.V., and Lykotrafitis, G. (2017). Modeling of the axon membrane skeleton structure and implications for its mechanical properties. PLoS Comput. Biol. *13*, e1005407.

Zhong, G., He, J., Zhou, R., Lorenzo, D., Babcock, H.P., Bennett, V., and Zhuang, X. (2014). Developmental mechanism of the periodic membrane skeleton in axons. eLife *3*, e04581.

**Cell Reports, Volume *22***

## Supplemental Information

# Super-Resolution Microscopy Reveals the Native Ultrastructure of the Erythrocyte Cytoskeleton

**Leiting Pan, Rui Yan, Wan Li, and Ke Xu**

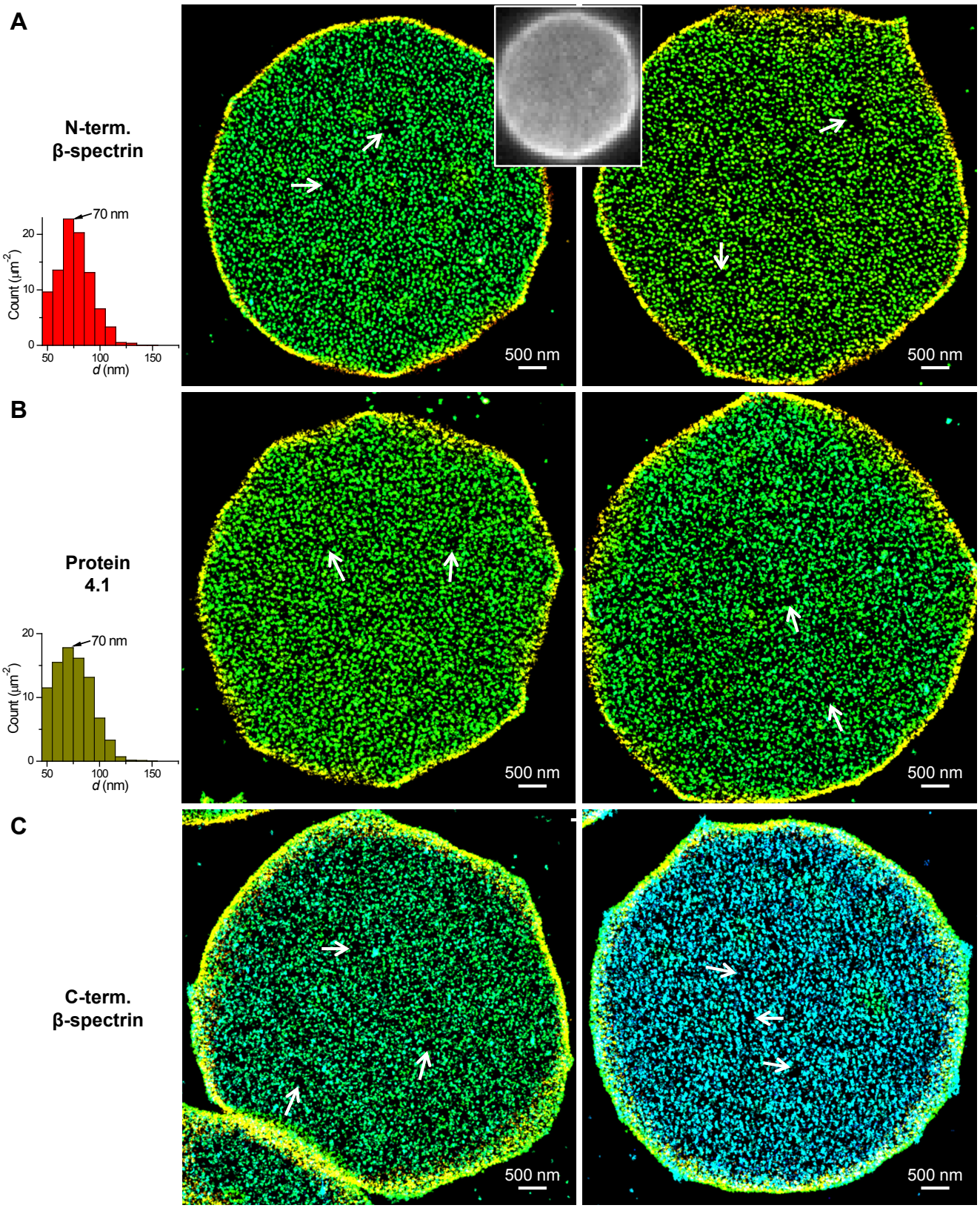


**Figure S1. Additional 3D-STORM results of β-spectrin and protein 4.1 in membrane-preserved erythrocytes.** Related to Figure 2. Distributions of distances between nearest neighbors are given for N-terminus of β-spectrin and protein 4.1 for the cells on the left. White arrows point to nanoscale voids. Inset gives a corresponding, diffraction-limited epifluorescence image: structural details, including the nanoscale voids, are unresolved.

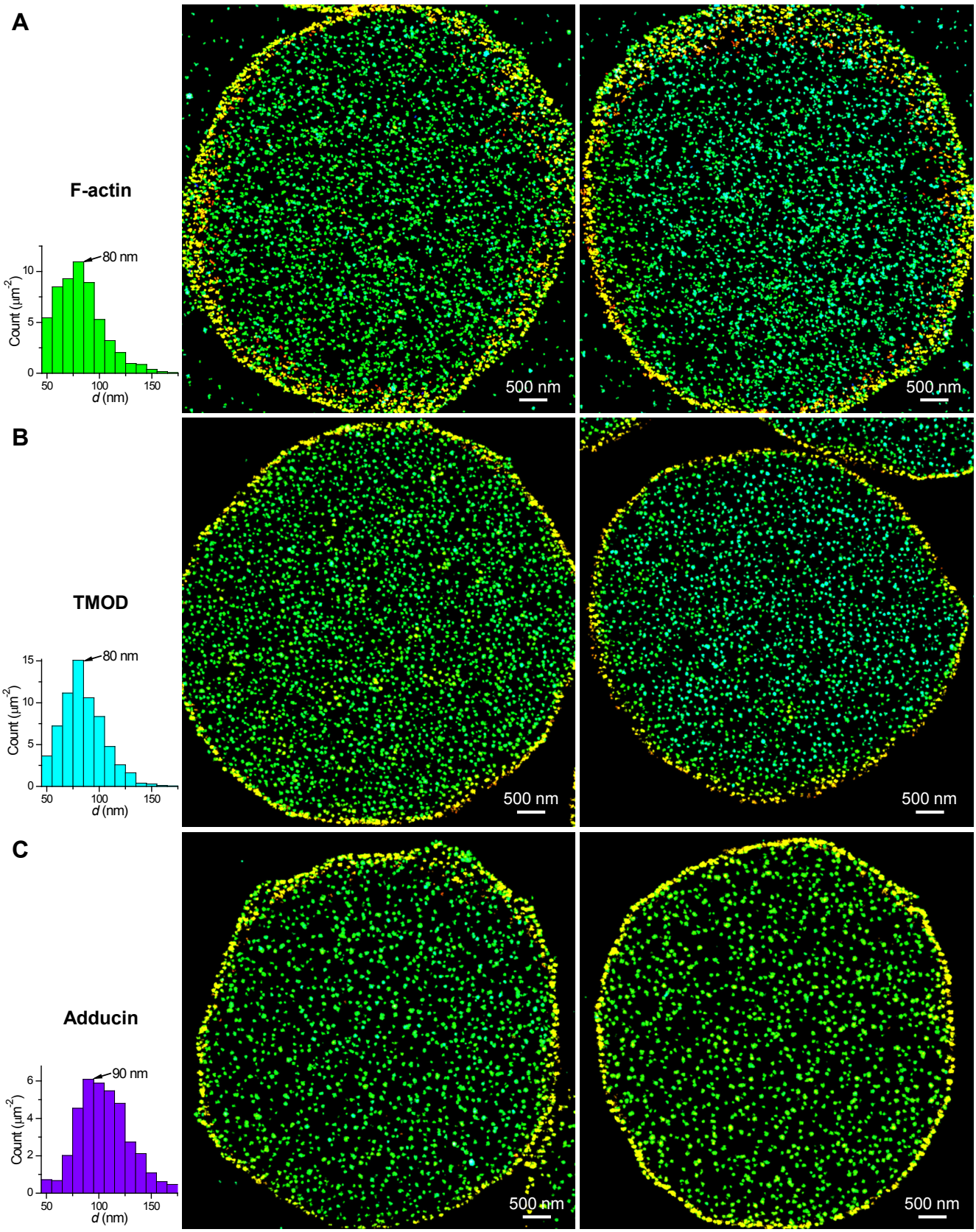


**Figure S2. Additional 3D-STORM images of 3D-STORM results of actin filaments and actin-capping proteins in membrane-preserved erythrocytes.** Related to Figure 3. Distributions of distances between nearest neighbors are given for the cells on the left.

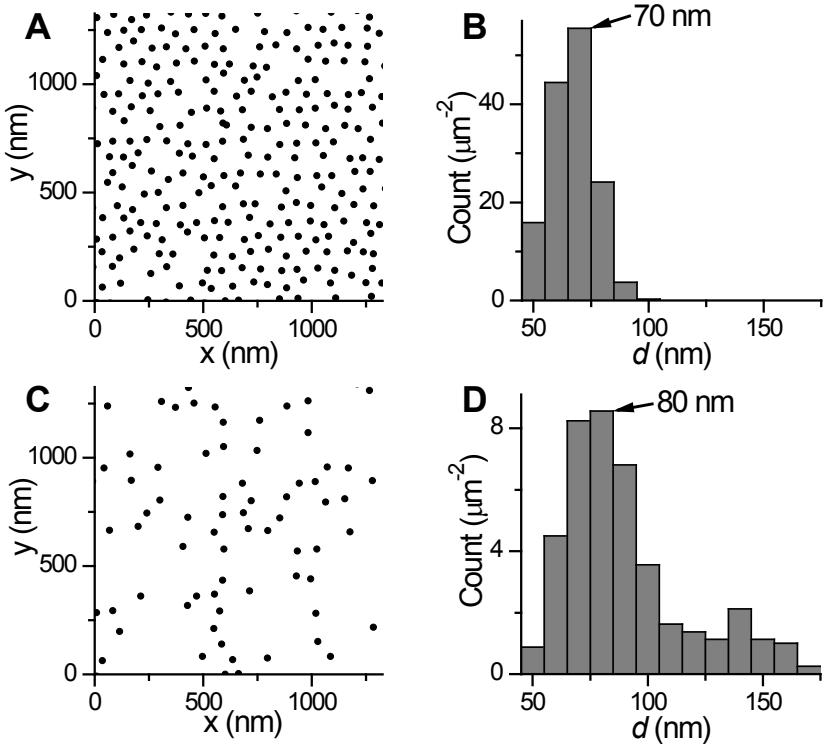


**Figure S3**. **Simulation of distances between nearest clusters.** Related to Figure 3.
(A) A part of the simulated data of junctional complexes based on a triangular lattice with 85 nm-long edges and an added random positional scattering of σ = 12 nm for each junction, with random removal of 10% of the junctions (90% occupancy).
(B) Distribution of junction-to-junction distances between nearest neighbors from the arrangement in (A).
(C and D) Same as (A and B), but with 75% of the junctions randomly removed (25% occupancy).

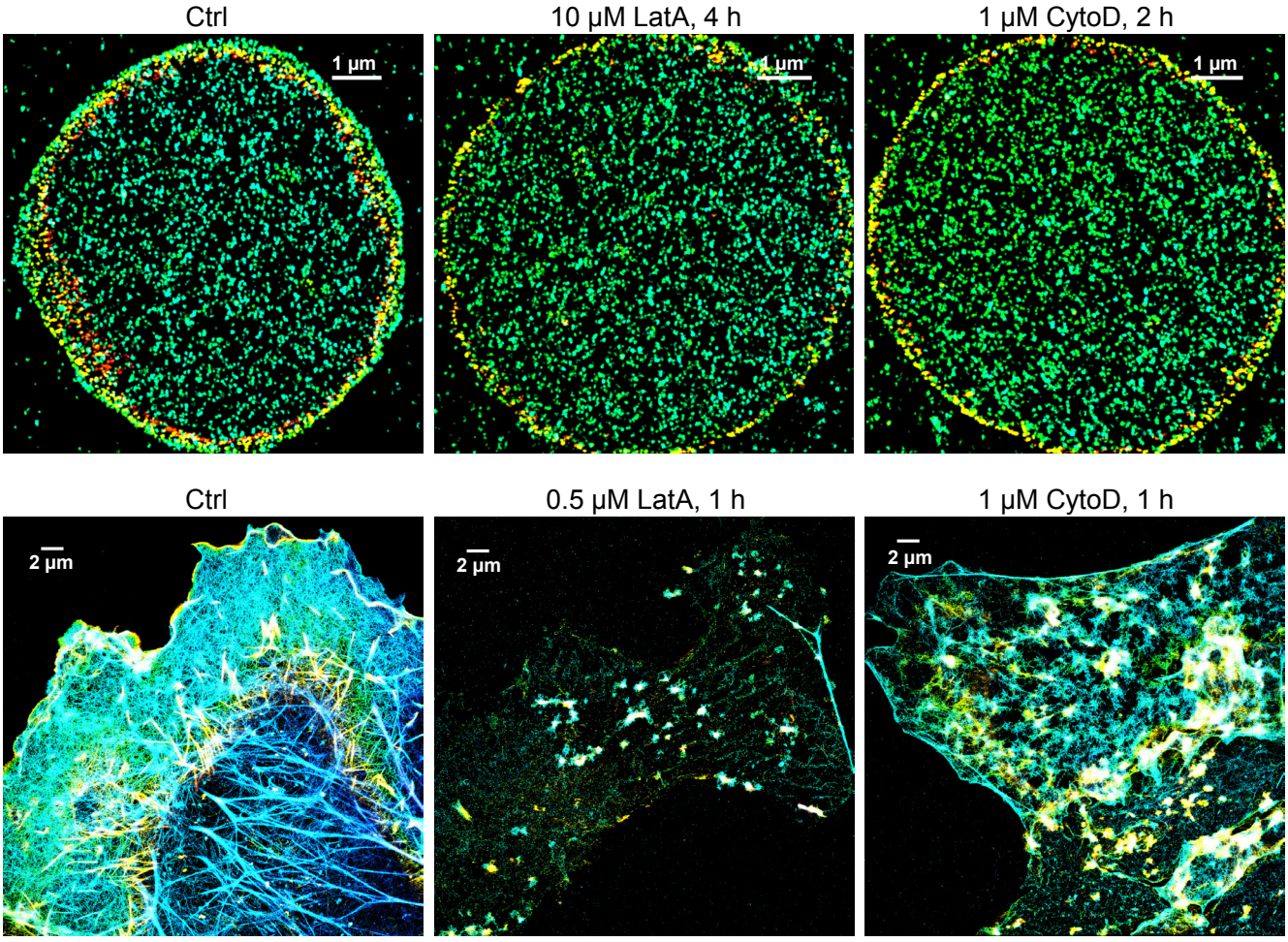


**Figure S4. The actin cytoskeleton after drug treatments.** Related to Figure 3. Erythrocytes were treated with 10 µM latrunculin A (LatA) for 3 h or 1 µM cytochalasin D (CytoD) for 1 h before depositing onto coverslips, and were further incubated for an additional 1 h in the presence of the drug before fixation. No noticeable structural changes were observed for the erythrocyte actin cytoskeleton. As a positive control, severe disruption of the actin cytoskeleton was observed for COS-7 cells with much lower drug concentrations and/or shorter treatment times (1 h treatments of 0.5 µM latrunculin A and 1 µM cytochalasin D).

**Supplemental Experimental Procedures**

**Reagents.** Poly-L-lysine solution (molecular weight: 70-150 kDa; P4707), saponin (S4521), bovine serum albumin (BSA) (A3059), cysteamine (30070), glucose oxidase (G2133), catalase (C30), MES (69892), and other general reagents were purchased from Sigma-Aldrich (St Louis, MO, USA). EM-grade paraformaldehyde (15714) and glutaraldehyde (16365) were from Electron Microscopy Sciences (Hatfield, PA, USA). CM-DiI (V-22888) and Alexa Flour 647-conjugated phalloidin (A22287) were from Invitrogen (Carlsbad, CA, USA). Primary antibodies used: Tropomodulin 1, mouse monoclonal, OriGene TA503146; protein 4.1R, rabbit polyclonal, Sigma HPA028414; adducin, rabbit polyclonal, Abcam ab51130; N-terminus of β-spectrin (actin-binding domain), rabbit polyclonal, Millipore ABT185; C-terminus of β-spectrin, mouse monoclonal, NeuroMab 73-374. Alexa Fluor 647-conjugated secondary antibodies (A31571 and A21245, Invitrogen) were used for single-color STORM and two-color STORM with CM-DiI. For other two-color STORM experiments, one target was labeled by an Alexa Fluor 647-labeled secondary antibody, and the second target was labeled by a secondary antibody conjugated with CF568 succinimidyl ester (#92131, Biotium, Fremont, CA, USA).

**Sample preparation.** Glass coverslips (dia. 12 mm) were acid washed and then coated with 0.1 mg/mL poly-L-lysine for 3 h at room temperature. After washing with deionized water, coverslips were dried and placed at the bottom of 24-well plates. 4 μL of fresh human blood was diluted in 6 mL phosphate-buffered saline (PBS) containing 10 mM glucose and 5 mg/mL BSA (PBS-GB), and washed once with PBS-GB by centrifugation at 1200 rpm for 5 min. The final suspension was adjusted to ~$3\times10^6$ cells/mL in PBS-GB. For adhesion-first experiments, 500 μL of the live-erythrocyte suspension was added to each well and allowed to adhere for ~10 min at room temperature. Unattached cells were removed by washing twice with PBS-GB. For immunofluorescence, attached cells were fixed in 4% paraformaldehyde for 10 min. Fixed cells were first blocked with a solution of 3% BSA and 0.05% Triton X-100 in PBS for 2 min, and then stained with corresponding primary and secondary antibodies in 3% BSA in PBS for 2 h and 40 min, respectively. For labeling of cell membrane, sample was then incubated with a CM-DiI staining solution for 20 min. For phalloidin labeling of actin filaments, attached cells were treated by 0.0015% saponin in cytoskeleton buffer (CB; 10 mM MES, pH 6.1, 150 mM NaCl, 5 mM EGTA, 5 mM glucose and 5 mM $MgCl_2$) (Xu et al., 2012) for 4 min, fixed in 2% glutaraldehyde in CB for 20 min, and reduced with a freshly prepared 0.1% sodium borohydride solution in PBS. Alexa Flour 647-conjugated phalloidin was applied at a concentration of ~0.4 μM for 40 min. For fixation-first experiments, live cells were suspended in a fixation solution of 3% paraformaldehyde and 0.1% glutaraldehyde in PBS for 10 min, centrifuged at 1200 rpm, and resuspended in PBS at ~$3\times10^6$ cells/mL. The fixed cells were allowed to adhere to the poly-L-lysine coated coverslips for ~4 h for subsequent immunofluorescence procedures as described above.

**STORM super-resolution microscopy.** 3D-STORM (Huang et al., 2008; Rust et al., 2006) was carried out on a home-built setup based on a modified Nikon Eclipse Ti-E inverted optical microscope using an oil-immersion objective (Nikon CFI Plan Apochromat λ, 100×, numerical aperture = 1.45), as described previously (Wojcik et al., 2015). Briefly, samples were mounted on glass slides using a standard STORM imaging buffer consisting of 5% (w/v) glucose, 100 mM cysteamine, 0.8 mg/mL glucose oxidase, and 40 μg/mL catalase in Tris-HCl (pH 7.5) (Huang et al., 2008; Rust et al., 2006). Lasers at 647, 560, and 405 nm were introduced into the sample through the back focal plane of the objective, and shifted towards the edge of the objective so that emerging light reached the sample at incidence angles slightly smaller than the critical angle, thus illuminating ~1 μm within the glass–water interface. A strong (~2 kW $cm^{-2}$) excitation laser of 647 nm (for Alexa Fluor 647) or 560 nm (for CF568 and CM-DiI) photoswitched most of the labeled dye molecules into a dark state, while also exciting fluorescence from the remaining, sparsely distributed emitting dye molecules for single-molecule localization. A weak 405-nm laser was used concurrently with either the 647- or 560-nm lasers to reactivate fluorophores into the emitting state. The power of the 405-nm laser (typical range 0-1 W $cm^{-2}$) was adjusted during image acquisition so that at any given instant, only a small, optically resolvable fraction of fluorophores was in the emitting state. A cylindrical lens was inserted into the imaging path to introduce astigmatism so that images of single molecules were elongated in opposite directions for molecules on the proximal and distal sides of the focal plane (Huang et al., 2008). Data was collected at 110 frames per second using an Andor iXon Ultra 897 EM-CCD camera, for a total of ~50,000 frames per image. 3D-STORM raw data were processed according to previously described methods (Huang et al., 2008; Rust et al., 2006), in which the centroid positions and ellipticities of the single-molecule images obtained in each frame were respectively used to deduce the lateral and axial positions of each molecule.

**Data analysis and modeling.** Two-dimensional cross-correlation analysis (Sengupta et al., 2011; Stone and Veatch, 2015) was performed by calculating the pairwise intermolecular distances between single molecules identified in the two color channels. Using a custom MATLAB program, a histogram was generated for the counts of molecule pairs that fell into different ranges of distances. This histogram was then normalized by histograms generated from multiple sets of molecules randomly distributed in the same area. The resultant normalized cross-correlation values (Figures 4E, 4J, and 4O) are thus

expected to show, in the limit of zero intermolecular distance, a value of <1 and >1 for excluding and co-localizing patterns in the two channels, respectively (e.g., Figures 4E and 4J). This initial value then tends to decay to 1 at increased intermolecular distances, and the decaying distance reflects the length scale over which the exclusion or co-localization occurs. Additional peaks and troughs may be observed for periodic patterns. For two independent structures in the two color channels, the normalized cross-correlation values are ~1 at all intermolecular distances (e.g., Figure 4O). To model the cytoskeleton network for comparison with experimental results, a triangular lattice with 85 nm-long edges was used as the starting point for all simulations. The vertices and edge centers were individually shifted randomly according to a two-dimensional Gaussian distribution of a standard deviation of $\sigma$ = 12 nm. Targets at the junctional complexes occupied a random fraction of the vertices (e.g., Figure S3). To simulate STORM data for comparison with cross-correlation analysis, single-molecule localizations were simulated as two-dimensional Gaussian distributions with a fixed standard deviation of 11 nm, corresponding to the localization uncertainty of STORM.